30th Congress of the International Council of the Aeronautical Sciences
DCC, Daejeon, Korea ; September 25-30, 2016

COMPUTATIONS OF SUPERSONIC LATERAL JET

Jinbum Huh*, Seungsoo Lee*
***Inha University**

Keywords: *Lateral jet, Jet interaction, Hit-to-kill vehicle*

Abstract

Lateral jets used in hit-to-kill vehicles induce complex jet interactions with external supersoni c flows. It is of paramount importance to analyze these jet interactions accurately in order to predict the missile performance. In this paper, we numerically analyzed the jet interaction on a supersonic generic missile by using an in-house CFD solver, MSAPv. Various numerical flux schemes were used to examine the complex flow field. The results at three conditions were computed and compared to the experimental results as well as each other. In addition, the complexity of the interacting flow was investigated using the behavior of vortical flow structure around the lateral jet.

1 Introduction

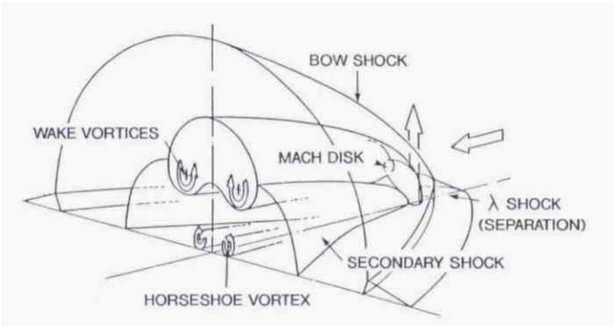

Fig. 1. Flow structure due to jet interaction [1]

Lateral jets used for missile control have advantages over conventional control surfaces especially at the high altitude. The advantages are fast response, and high maneuverability. Because of these advantages, the lateral jet is widely used in hit-to-kill vehicles, such as THAAD and PAC-3.

The lateral jet, however, leads to complicated jet interaction with the free-stream especially in the supersonic region, which is depicted in Fig. 1. Due to low pressure of the free-stream, the lateral jet experiences expansion and acceleration to high supersonic speed, which results in a barrel shock and a Mach disk. This barrel shock obstructs the free-stream and induces a bow shock. The bow shock interacts with the boundary layer of the missile, consequently triggers flow separation and a λ-shock. In addition, the wake vortices to the rear of the barrel shock forms kidney vortex pairs.

The accurate analysis of the jet interaction is known to be difficult. As described earlier, the jet interaction involves shocks, expansion waves and vortices. Especially the Mach disk, which is a strong normal shock, easily induces numerical instabilities. Various numerical flux schemes are used to circumvent the numerical difficulties. Sanders's H-correction[2] controls dissipation by using entropy corrections of the neighboring cells. RoeM scheme[3] resolves numerical instability by introducing Mach number-based functions.

Understanding the jet interaction is important to predict the aerodynamic characteristics of the missile. The separated flow in the front of the barrel shock generates a horse shoe vortex that increases the surface pressure. On the other hands, another horse shoe vortex that emanates from the rear of the barrel shock makes a recirculation zone that drops the surface pressure. These cause a nose down moment of the missile. The accurate analysis of the jet interaction, therefore, is necessary to predict the missile maneuver at the terminal stage.

Wallis[4] experimentally studied the jet interaction on a flat plate at supersonic speeds. The test was conducted with/without secondary jets in various flow conditions. Wallis investigated jet interaction flow structures by using Schlieren photographs and surface pressures distributions. Viti[5] numerically analyzed Wallis's wind tunnel test. Viti focused on explaining the flow physics of the jet interaction in detail. In his study, it is well described how shocks, expansions and free-stream interact. Stahl[6] conducted a wind tunnel test of the jet interaction on a generic missile model. The test was carried out with not only cold air jet but also hot gas jet. Gnemmi[7] performed a numerical study of Stahl's experiment and compared the aerodynamic coefficients of the various solvers.

In this paper, we numerically study the jet interactions with the supersonic free-stream over a generic missile by using an in-house solver, MSAPv[8]. The model geometry and test condition are the same as the Stahl's wind tunnel test[6]. We examine the detailed flow structure of the jet interaction and compare the results of various flux functions. Furthermore, we analyze the results of three jet conditions. Finally, we investigate the vortical structure near the lateral jet. These numerical analyses are conducted with steady state and inert gas assumption.

2 Numerical method

2.1 Governing equations

The three-dimensional Reynolds averaged Navier-Stokes(RANS) equations are used in MSAPv as the governing equations, and can be written as

$$\frac{\partial W}{\partial t}+\frac{\partial E}{\partial x}+\frac{\partial F}{\partial y}+\frac{\partial G}{\partial z}=\frac{\partial E_v}{\partial x}+\frac{\partial F_v}{\partial y}+\frac{\partial G_v}{\partial z} , \qquad (1)$$

where W is the conservative flow variable vector. While E, F and G are the inviscid flux vectors, and E_v, F_v and G_v are the viscous flux vectors of each direction. The solution vector and the flux vectors are defined by

$$W=\begin{bmatrix}\rho & \rho u & \rho v & \rho w & e\end{bmatrix}^T , \qquad (2)$$

$$E=\begin{bmatrix}\rho u & \rho u^2+p & \rho uv & \rho uw & (e+p)u\end{bmatrix}^T , \qquad (3)$$

$$F=\begin{bmatrix}\rho v & \rho vu & \rho v^2+p & \rho vw & (e+p)v\end{bmatrix}^T , \qquad (4)$$

$$G=\begin{bmatrix}\rho w & \rho wu & \rho wv & \rho w^2+p & (e+p)w\end{bmatrix}^T , \qquad (5)$$

$$E_v=\begin{bmatrix}0 & \tau_{xx} & \tau_{xy} & \tau_{xz} & \Omega_x\end{bmatrix}^T , \qquad (6)$$

$$F_v=\begin{bmatrix}0 & \tau_{yx} & \tau_{yy} & \tau_{yz} & \Omega_y\end{bmatrix}^T , \qquad (7)$$

$$G_v=\begin{bmatrix}0 & \tau_{zx} & \tau_{zy} & \tau_{zz} & \Omega_z\end{bmatrix}^T , \qquad (8)$$

where τ_{ij} and Ω_i are the stress tensor, and the total energy flux vector, respectively. The governing equations are discretized with a finite volume method(FVM). The inviscid flux is computed with Roe's flux[9], RoeM flux[3], and HLLE flux[10,11]. Van Leer's MUSCL extrapolation[12] is used to obtain second order spatial accuracy and Van Albada's limiter is used to maintain Total Variation Diminishing(TVD) property even if the shock exists. The gradient theorem over auxiliary cell is chosen for computing the gradient of flow variables. The approximate factorization-alternative direction implicit(AF-ADI) scheme[13] is used to advance the solutions in time. The Spalart-Allmaras's 1-Eq turbulence model is selected[14] to compute the turbulent viscosity.

2.2 Numerical flux scheme

The jet interaction shows the complicated flow structure such as a barrel shock, a Mach disk and expansion waves. The Roe scheme is a widely used and reliable scheme, but showed a numerical instability near strong normal shocks. Therefore, we choose three numerical flux schemes and compare their results.

2.2.1 Roe scheme with H-correction

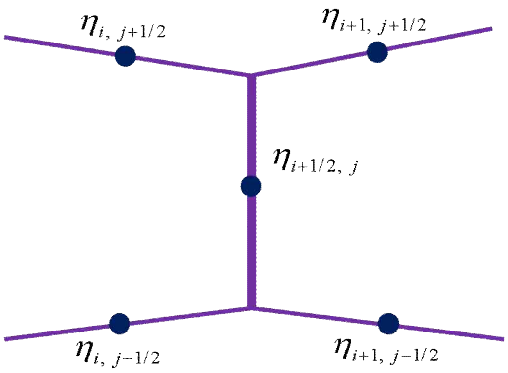

Fig. 2. Cell interface

The Roe scheme[9] based on an approximated Riemann solver defines the numerical flux as,

$$\tilde{F}_{i+1/2} = \frac{1}{2}\left[\hat{F}_{i+1} + \hat{F}_i - |A|\left(W_{i+1} - W_i\right)\right],$$
$$A = \frac{\partial F}{\partial W}. \qquad (9)$$

In this formula, the Jacobian matrix, A has to satisfy the hyperbolicity, consistency and conservation. To satisfy these conditions, the Roe's averaged variables are used. The Roe scheme, however, doesn't have enough cross dissipation normal to the shock. Non-physical results, such as carbuncle phenomena, may occur. Thus, various entropy correction schemes were proposed to alleviate this problem. In this study, we choose Sanders's H-correction[2]. This method calculates one-dimensional entropy correction, η at cell interface, and chooses η^H as the maximum η value over the neighboring cells. Figure 2 shows the neighboring cells at the cell interface. The figure explains why this method is called as H-correction. From this simple procedure, the multi-dimensional dissipation can be modified. With η^H, the eigenvalues of the Jacobian matrix are modified with Eq. (10)

$$\eta_{i+1/2,\ j} = \frac{1}{2}\max_l\left[\left|\lambda_l\left(U_{i+1}\right) - \lambda_l\left(U_i\right)\right|\right],$$

$$\eta^H_{i+1/2,\ j} = \max\begin{bmatrix}\eta_{i+1/2,j}, \eta_{i,j+1/2}, \eta_{i,j-1/2}, \\ \eta_{i+1,j+1/2}, \eta_{i+1,j-1/2}\end{bmatrix}, \qquad (10)$$

$$\left|\tilde{\lambda}_l\right| = \max\left[\left|\lambda_l\right|, \eta^H\right].$$

2.2.3 RoeM scheme

RoeM scheme[3] suggests the Mach number-based function, f to control the instability. In the similar way, a function g is introduced to control density perturbation. The numerical flux by RoeM scheme is defined by

$$\tilde{F}_{i+1/2} = \frac{b_1 \times \hat{F}_{i+1} - b_2 \times \hat{F}_i}{b_1 - b_2} + \frac{b_1 \times b_2}{b_1 - b_2}\Delta Q^* - g\frac{b_1 \times b_2}{b_1 - b_2} \times \frac{1}{1 + \left|\hat{M}\right|} B\Delta Q,$$

$$f = \begin{cases} 1 & \hat{u}^2 + \hat{v}^2 = 0 \\ \left|\hat{M}\right| & \text{elsewhere} \end{cases},$$

$$h = 1 - \min\begin{bmatrix} P_{i+1/2,j}, P_{i,j+1/2}, P_{i,j-1/2}, \\ P_{i+1,j+1/2}, P_{i+1,j-1/2} \end{bmatrix}, \qquad (11)$$

$$P_{i+1/2,j} = \min\left(\frac{P_{i,j}}{P_{i+1,j}}, \frac{P_{i+1,j}}{P_{i,j}}\right),$$

$$g = \begin{cases} \left|\hat{M}\right|^{1-\min\left(\frac{P_{i,j}}{P_{i+1,j}}, \frac{P_{i+1,j}}{P_{i,j}}\right)} & M \neq 0 \\ 1 & M = 0 \end{cases}.$$

RoeM scheme is designed to cure the instability of the shock or expansion wave, and has advantage of preserving the total enthalpy.

2.2.4 HLLE scheme

The HLLE scheme [10,11] approximates the solution of Riemann problem with three states separated by two discontinuities. The numerical flux function is defined by

$$\tilde{F}_{i+1/2} = [(b^+_{i+1/2}F(Q_i) + b^-_{i+1/2}F(Q_{i+1})) + (b^+_{i+1/2}b^-_{i+1/2}\left(Q_{i+1} - Q_i\right))] / (b^+_{i+1/2} - b^-_{i-1/2}),$$

$$b^+_{i+1/2} = \max\left(\bar{u} + \bar{c},\ u_{i+1} + c_{i+1}\right), \qquad (12)$$

$$b^-_{i+1/2} = \min\left(\bar{u} - \bar{c},\ u_i + c_i\right),$$

where $\bar{u}$ and $\bar{c}$ mean Roe's averaged values. This scheme shows good robustness at the back of strong shock or expansion wave. Large error may occur due to a lack of the information of the contact discontinuity.

3 Analysis conditions

3.1 Geometry & flow conditions

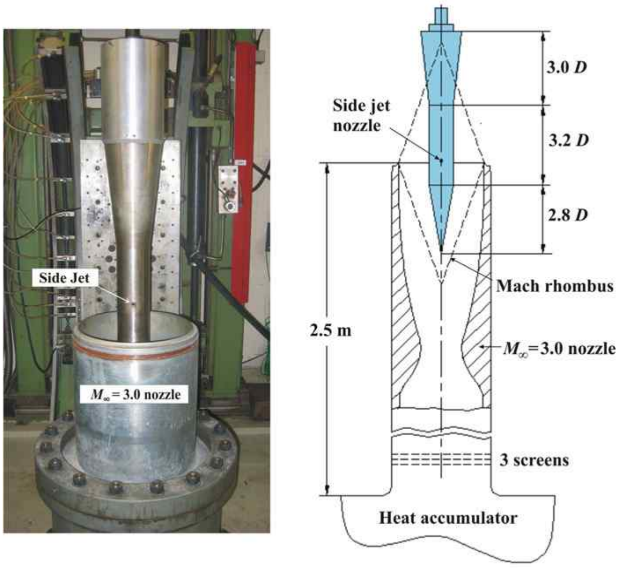

Fig. 3. Model and test section

Figure 3 shows a generic missile model and the test section of the VMK supersonic wind tunnel in Cologne[6]. The generic missile consists of a cone-cylinder-flare body and a lateral jet nozzle. The diameter of the cylinder is $D = 90\,\text{mm}$ and the base diameter is $1.66\,D$. The lateral jet nozzle diameter is $d_{jet} = 4.6\,\text{mm}$ and is located at $\varphi = 180°$, $x/D = 4.3$. A Mach rhombus shown Fig. 3(right) occurs in the experiment due to a truncated wind tunnel nozzle. Because the nozzle is not modeled in the computations, the Mach rhombus is not captured in the numerical results.

Table 1 shows the detailed flow conditions. The Mach number of the free-stream is $M_\infty = 3.0$, and the Mach number at the lateral jet exit is $M_{jet} = 1.0$. The Reynolds number, Re_D, is based on the cylinder diameter. T_∞ and T_{jet} are the temperatures of the free-stream and the jet exit, respectively. P_∞ is the static pressure of the free-stream and P_K is the stagnation pressure of the jet. Case 3 was experimented with a hot gas jet which is a non-equilibrium and multi-species gas. In the numerical analysis, however, the jet is assumed to be a single-species gas.

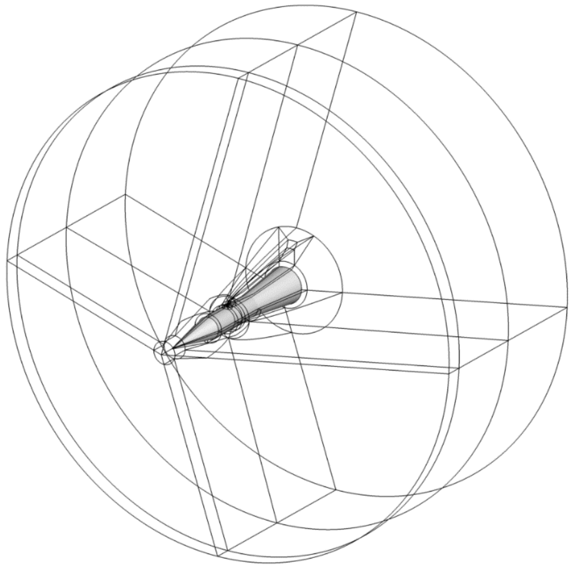

Fig. 4. Topology of grid system

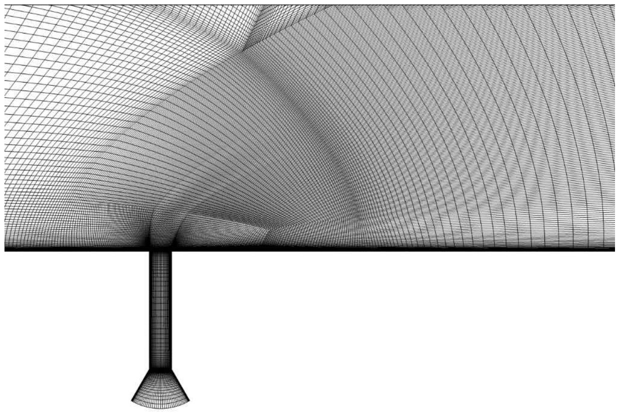

Fig. 5. Close-up view of grid at symmetric surface

3.2 Grid system

The total grid system consists of 64 blocks, 12.1 million cells. Figure 4 presents the total grid system over the generic missile. The grid

Table 1. Flow conditions

	M_∞	M_{jet}	T_∞ (K)	T_{jet} (K)	P_∞ (bar)	P_K (bar)	P_K/P_∞	Re_D
Case 1	3.0	1.0	105	244	0.545	120	220	14.0×10^6
Case 2			105	244	0.923	120	130	25.0×10^6
Case 3			105	2058	0.545	120	220	14.0×10^6

topology is composed in consideration of the flow field. Since the free-stream is supersonic, the inflow far-field is located close to the nose, and the exit far-field is located at the base area of the missile.

Figure 5 shows the symmetric surface near the lateral jet nozzle. The grid points are clustered near the Mach disk. The nozzle throat is included to take account of the nozzle boundary layer. At the lateral jet inflow boundary surface, the total pressure and the total temperature are specified, and the inflow velocity is computed. To assure the resolution of the turbulent boundary layer flow, the first mesh height from the surfaces satisfies $y^+ < 1$.

4 Results

4.1 Comparison of numerical flux schemes

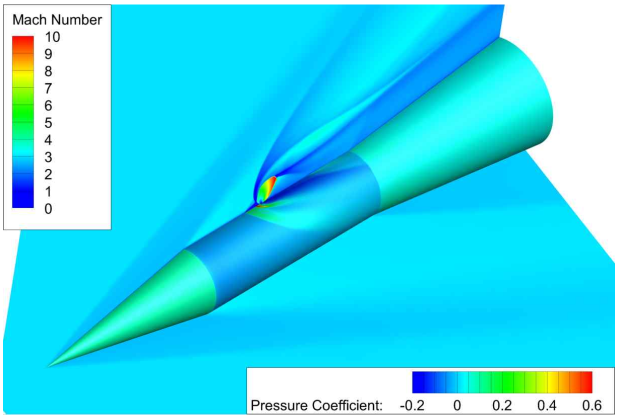

Fig. 6. Mach contour and C_P contour

Figure 6 presents overview results of the jet interaction simulation by using Roe scheme with H-correction. While the Mach contour are presented at the symmetric surface, the pressure coefficient contour are presented at the missile surface. On the Mach contour, the shock structure including the barrel shock are cleary captured. At the missle surface, on the other hand, the horse shoe pattern can be seen clearly as well. Figure 7 compares the shock structure of the numerical and experimental results near the jet exit. The numerical results, presented in Fig. 7(b)-(d), show the similar Mach contours, and describe the barrel shock and the Mach disk clearly. It is shown that all flux schemes predict

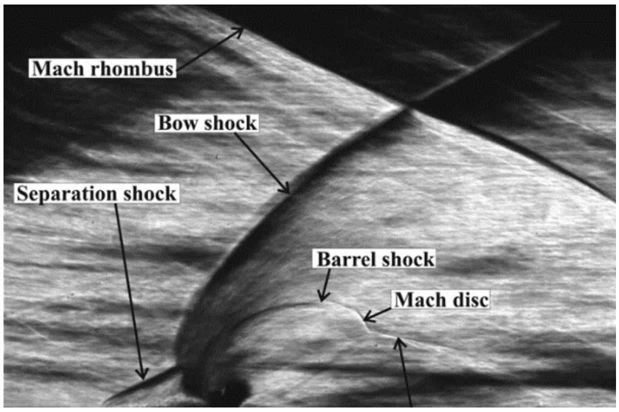

(a) Schliren visualization

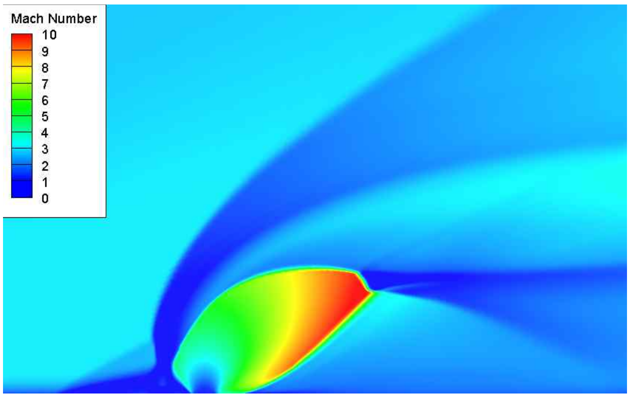

(b) Roe scheme with H-correction

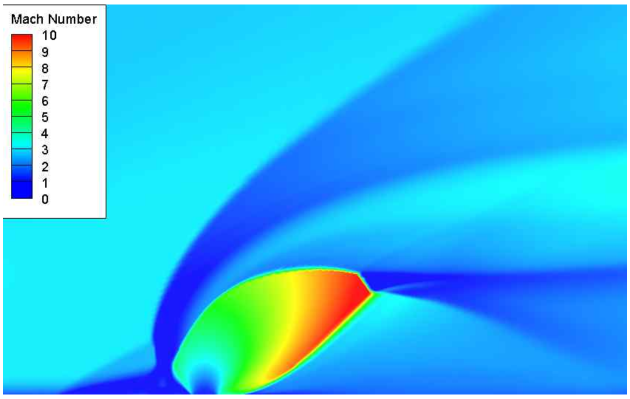

(c) RoeM scheme

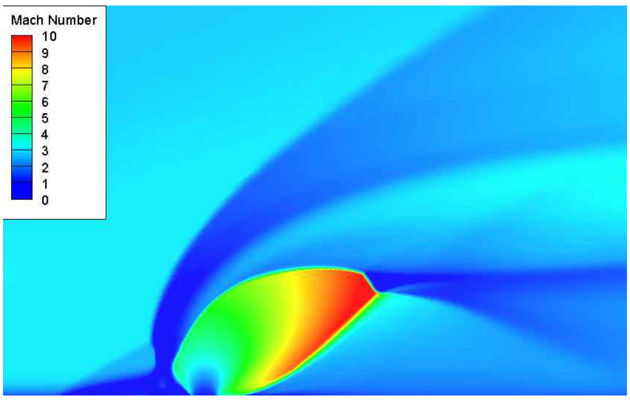

(d) HLLE scheme

Fig. 7. Shock structure on the symmetric surface

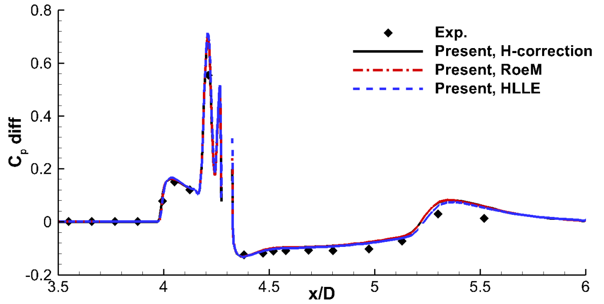

(a) φ =180°

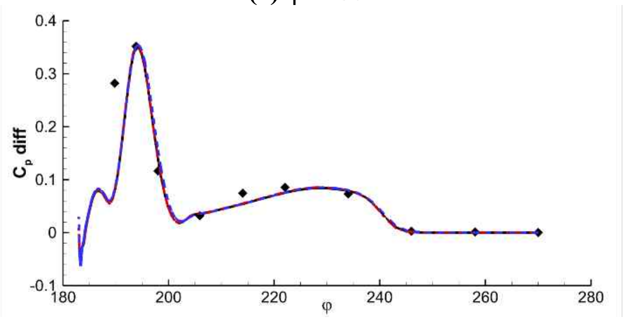

(b) x/D = 4.3

Fig. 8. Differential pressure coefficient distribution

the Mach disk and shock structure without numerical instability. Figure 7(a) presents the Schlieren image of the wind tunnel test. The barrel shock sizes and the positions of the numerical and experiment results are similar to each other. As stated eariler, the Mach rhombus is only shown at Fig. 7(a). This difference is induced by the truncated wind tunnel exit.

Figures 8(a), (b) show the differential pressure coefficient, $C_P\,\mathrm{diff.}$, distributions along the longitudinal direction at the symmetric surface, φ=180°, and the circumferential direction at a longitudinal location, x/D=4.3. The $C_P\,\mathrm{diff.}$ is defined by the difference between with/without lateral jet. The $C_P\,\mathrm{diff.}$ calculated by the all three flux schemes are nearly coincident with each other. All computational results show good agreement with the experimental results such as separation region or peak pressure location.

Thus, it is confirmed that the CFD has sufficient fidelity to analyze the jet interaction flow. Furthermore, all schemes predict the similar results in the Mach contour as well as $C_P\,\mathrm{diff.}$ distribution. Since there is no critical difference among the results with the flux schemes, the following analyses are conducted with the Roe scheme with H-correction only.

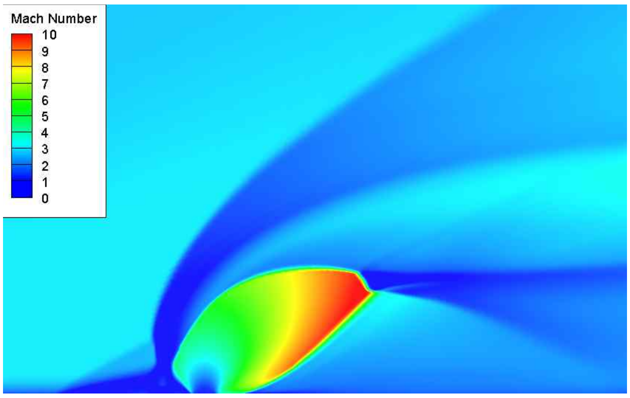

(a) Case 1

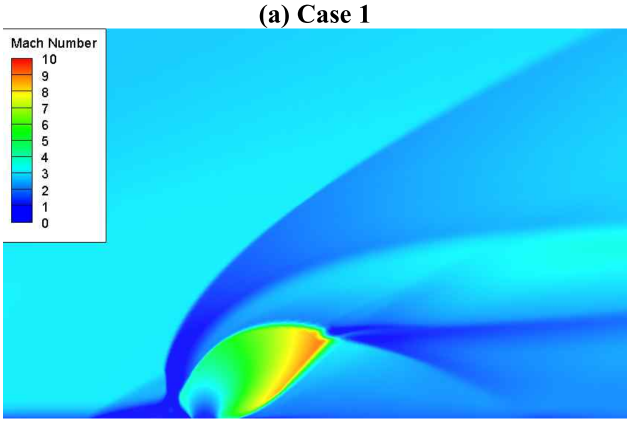

(b) Case 2

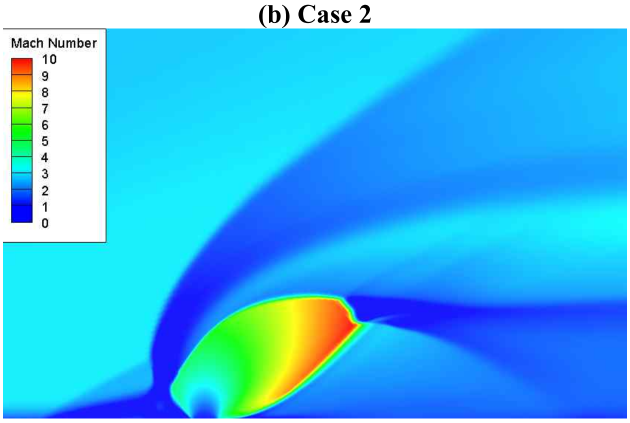

(c) Case 3

Fig. 9. Mach Contours as jet conditions

4.2 Comparison of jet conditions

Figure 9 shows the Mach contours with different jet conditions. The pressure ratio of Case 2 is lower than those of others. The shock

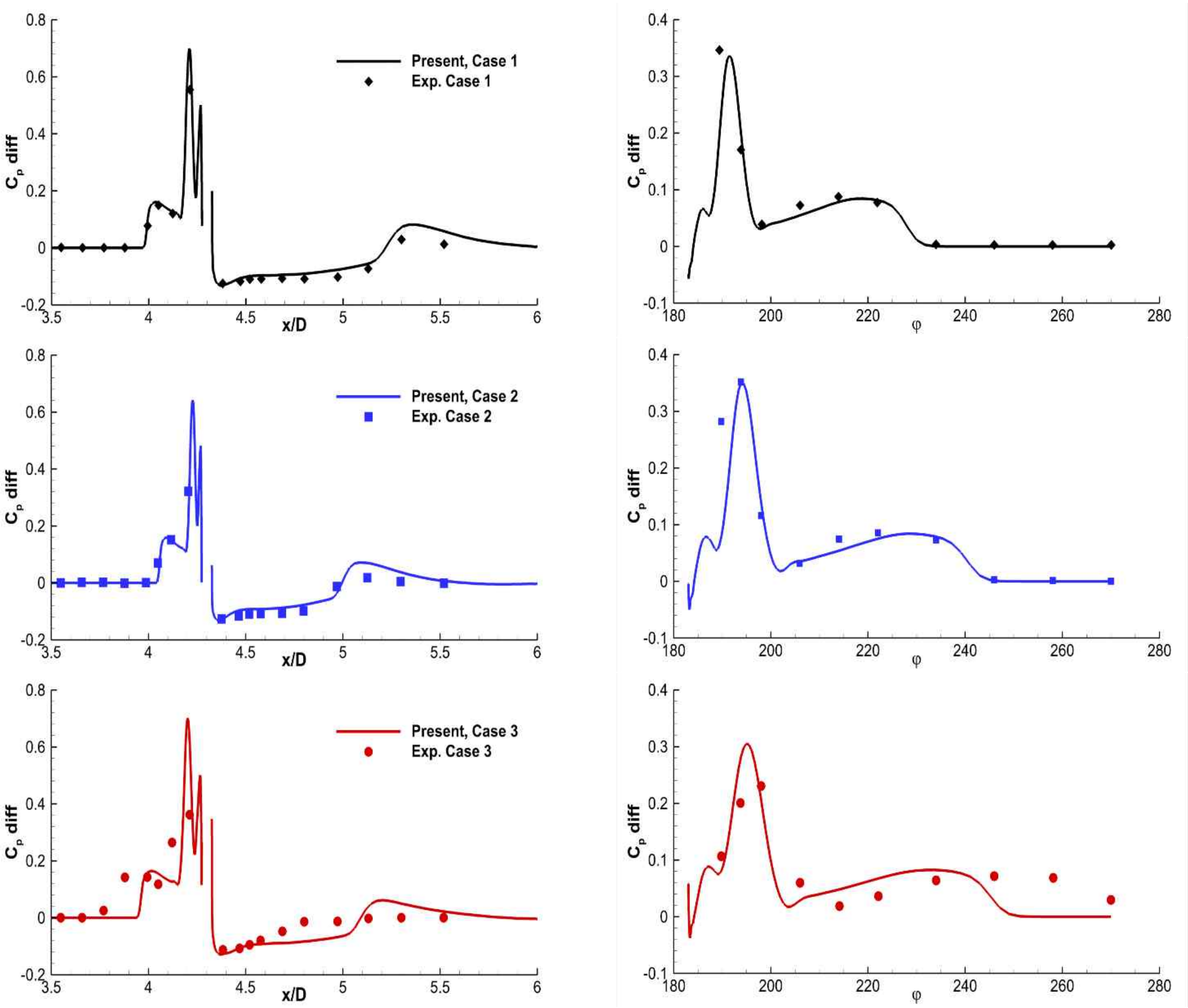

(a) φ =180° (b) x/D =4.3°

Fig. 10. Differential pressure coefficient distributions as jet condition

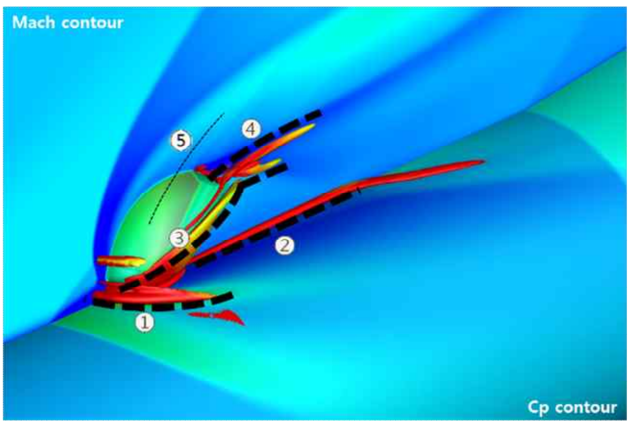

Fig. 11. Vortex core structure

structure of Case 2 is quite different from other results such as in the size of the barrel shock. On the other hand, Case 3 shows the similar results with Case 1, but not with Case 2. The jet temperature of Case 3 is higher than those of Cases 1 and 2. Thus, it is concluded that the structure of the jet interaction depends primarily on the jet pressure ratio, and that the jet temperature has little effect on the flow structure.

Figure 10 presents C_P diff. distributions of the jet conditions. Cases 1 and 2 show good agreement with the wind tunnel test. The result of Case 3, however, do not agree with the experiment. This discrepancy comes from the fact that CFD analysis assumes a single species jet. We can confirm that multi species effect can be important in hot gas jet computations.

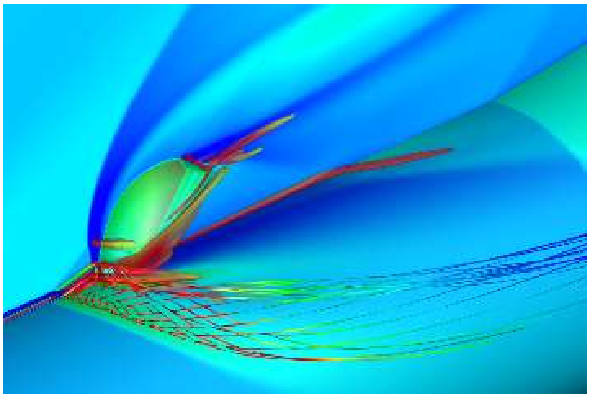

(a) Outer separation vortex

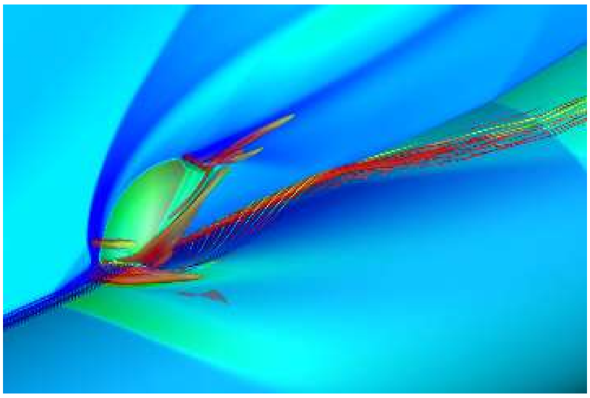

(b) Surface vortex

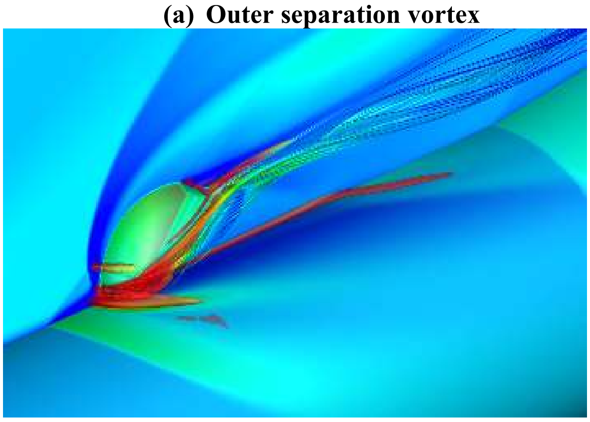

(c) Inner separation vortex

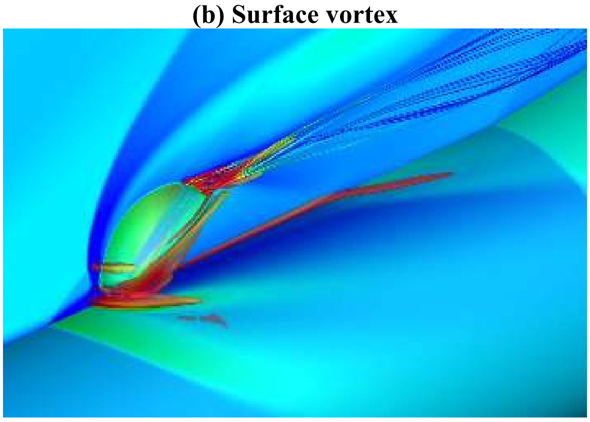

(d) Mach disk vortex

Fig. 12. Vortex flow around the vortex cores

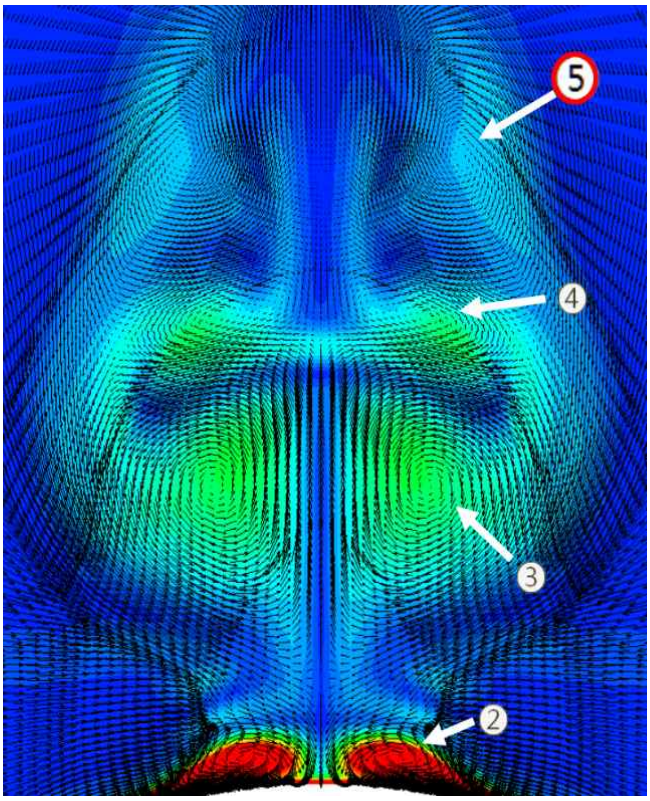

Fig. 13. Velocity vector at cross section at x/D=5.3

4.3 Vortex core

Figure 11 presents the barrel shock and 5 main vortex cores. The vortex cores are represented as dotted line. The barrel shock is expressed by iso-surfaces of Mach number 4.1 and the vorticity is calculated by using the λ_2 method[15]. Since the fifth vortex core is too weak to be identified by the λ_2 method, it is marked with a thin dotted line.

Figure 12(a)-(d) shows each vortex core and the streamlines associated with the core. The first core is located outside of the horseshoe vortex, and the second core is near the surface behind the jet exit. These two vortex cores generate separation and a recirculation region. Thus, the nose down effect is induced by these cores. Figure 12(c) shows the third vortex core which surrounds the barrel shock. This vortex core induces the inner horse shoe vortex. The forth vortex core locates behind the Mach disk. As shown in Fig. 12(d), the flow passing the Mach disk is influenced by this vortex core.

Figure 13 presents the velocity vector plot at x/D=5.3 plane. The kidney vortex pairs are captured clearly. There is the fifth vortex core at the top.

5 Conclusions

In this study, we perform numerical analysis of the jet interactions at the supersonic speeds. We use various flux schemes in the computations. All schemes are able to capture the complex jet interaction and their results match well with the experimental data. From the results of various jet conditions, it is found that the jet interaction structure depends primarily on the jet pressure ratio. In addition, it is found that the multi species effect should be included in analyzing the hot gas jet. Finally, the vortex cores and their effect on the flow are examined to understand the vortex flow structure.

Acknowledgment

This work was conducted at High-Speed Vehicle Research Center of KAIST with the support of Defense Acquisition Program Administration (DAPA) and Agency for Defense Development (ADD).

References

[1] Champigny, P., and Lacau, R.G., "Lateral jet control for tactical missiles," Special Course on Missile Aerodynamics, AGARD-R-804, Paper No. 3, 1994.

[2] Sanders, R., "Multidimensional dissipation for upwind schemes: stability and applications to gas dynamics," *Journal of Computational Physics*, Vol. 145, No. 2, pp. 511-537, 1998.

[3] Kim, S.S., Kim, C., Rho, O.H., and Hong, S.K., "Cures for the shock instability: Development of a shock-stable Roe scheme," *Journal of Computational Physics*, Vol. 185, No. 2, pp. 342-374, 2003.

[4] Wallis, S., "Innovative transverse jet interaction arrangements in supersonic crossflow," M.S. Thesis, Virginia Tech, December 2001.

[5] Viti, V., "Detailed flow physics of the supersonic jet interaction flow field," *Physics of fluids*, Vol. 21, No. 1, pp. 1-16, 2009.

[6] Stahl, B., Emunds, H., and Gülhan, A.," Experimental investigation of hot and cold side jet interaction with a supersonic cross-flow," *Aerospace Science and Technology*, Vol. 13, No. 1, pp. 488-496, 2009.

[7] Gnemmi, P., Gruhn, P., Leplat, M., Nottin, C., and Wallin, S., "Computation validation on lateral jet interactions at supersonic speeds," *International Journal of Engineering Systems Modelling and Simulation 47*, Vol. 5, No. 1-3, pp. 68-83, 2013.

[8] Lee, S., and Choi, D., "On coupling the Reynolds-averaged Navier–Stokes equations with two-equation turbulence model equations," *International journal for numerical methods in fluids*, Vol. 50, No. 2, pp. 165-197, 2006.

[9] Roe, P.L., "Approximate Riemann solvers, parameter vectors, and difference schemes," *Journal of computational physics*, Vol. 43, No. 2, pp. 357-372, 1981.

[10] Harten, A., Lax, P.D., and van Leer, B., "On upstreaming differencing and Godunov-type schemes for hyperbolic conservation laws," *SIAM Review.*, Vol. 25, No. 01, pp. 35-61, 1983.

[11] Einfeldt, B., "On Godunov-type methods for gas dynamics," *SIAM Journal on. Numerical Analysis*, Vol. 25, No. 2, pp. 294-318 1988.

[12] Van Leer, B., "Towards the ultimate conservative difference scheme. II. Monotonicity and conservation combined in a second-order scheme," *Journal of computational physics*, Vol. 14, No. 4, pp. 361-370, 1974.

[13] Beam, R.M., and Warming, R.F., "Implicit numerical methods for the compressible Navier-Stokes and Euler equations," *Von Karman Institute for Fluid Dynamics Lecture Series*, 1982.

[14] Spalart, P.R., and Allmaras, S.R., "A one-equation turbulence model for aerodynamic flows," *30th Aerospace Sciences Meeting & Exhibit*, Reno, AIAA Paper 92-0439, pp. 1-22, 1992.

[15] Jeong, J., and Hussain, F., "On the identification of a vortex," *Journal of fluid mechanics*, Vol. 285, No. 1, pp. 69-94, 1995.

Contact Author Email Address

Mail to: slee@inha.ac.kr

Copyright Statement